

# Analysing large scale structure: II. Testing for primordial non-Gaussianity in CMB maps using surrogates

Christoph R ath <sup>\*</sup> and Peter Schuecker

*Centre for Interdisciplinary Plasma Sciences (CIPS)/  
Max-Planck-Institut f ur extraterrestrische Physik (MPE), Garching, Germany*

Accepted ... Received ...; in original form ...

## ABSTRACT

The identification of non-Gaussian signatures in cosmic microwave background (CMB) temperature maps is one of the main cosmological challenges today. We propose and investigate alternative methods to analyse CMB maps. Using the technique of constrained randomisation we construct surrogate maps which mimic both the power spectrum *and* the amplitude distribution of simulated CMB maps containing non-Gaussian signals. Analysing the maps with weighted scaling indices and Minkowski functionals yield in both cases statistically significant identification of the primordial non-Gaussianities. We demonstrate that the method is very robust with respect to noise. We also show that Minkowski functionals are able to account for non-linearities at higher noise level when applied in combination with surrogates than when only applied to noise added CMB maps and phase randomised versions of them, which only reproduce the power spectrum.

**Key words:** Cosmology: methods – data analysis techniques: image processing – large scale structure of the universe, cosmic microwave background

## 1 INTRODUCTION

A fundamental question of cosmology is whether the observed fluctuations were Gaussian or non-Gaussian when they were formed. This gives important information about the nature of the fluctuations and how they were generated (e.g. inflationary or ekpyrotic/cyclic processes, moving cosmic strings etc.). A measurement of non-Gaussianity from the large scale structure of galaxies is, however, difficult because the non-linear gravitational collapse itself generates non-Gaussianity from Gaussian signals. Therefore, measurements of the temperature anisotropies of the cosmic microwave background (CMB) are regarded as the best way to identify the true nature of primordial fluctuations. Fundamental limitations of these measurements are cosmic variance on large scales and the central limit theorem on small scales.

In single field inflationary models (Guth 1981; Linde 1982; Albrecht & Steinhardt 1982), incorporating cold dark matter, the distribution of temperature fluctuations in the CMB should be a homogenous isotropic almost Gaussian random field. While for Big-Bang-inspired inflationary scenarios non-Gaussian contributions of  $10^{-5}$  relative to the leading Gaussian term are expected, for M-theory based

ekpyrotic/cyclic scenarios non-Gaussian contributions of higher order are expected to be exponentially suppressed yielding a kind of super-Gaussianity (Steinhardt & Turok 2002). Multi field inflationary models, on the other hand, open the door to the generation of primordial non-Gaussianities because of the possible non-linear couplings of the fields (Bernardeau & Uzan 2002). Another class of theories predict the formation of topological defects such as cosmic strings, monopoles or textures. According to these theories the CMB temperature fluctuations are expected to be non-Gaussian possessing steep gradients or 'hot-spots' of emission (Bouchet, Bennett & Stebbins 1988; Turok 1996). The need for very powerful statistical measures for detecting non-Gaussian signatures in the CMB maps is obvious and has led to the development of many different analysing techniques. The bispectrum (e.g. Verde et al. 2000; Sandvik & Magueijo 2001) and trispectrum (e.g. Verde & Heavens 2001; Hu 2001) as well as phase mapping techniques (Chiang, Coles & Naselsky 2002; Chiang, Naselsky & Coles 2002) rely on a Fourier-based analysis of CMB maps. The application of *local* Fourier techniques in the form of wavelets turned out to detect non-Gaussianities with high significance (Hobson, Jones & Lasenby 1999; Cay on et al. 2001; Barreiro & Hobson 2001).

Non-Gaussian signatures have also been identified by quantifying the morphology of CMB maps. In this

<sup>\*</sup> E-mail: cwr@mpe.mpg.de

context it has been proposed by Coles & Barrow (1987) and Coles (1988) to calculate the genus (Euler characteristic) of an excursion set. Other measurable topological quantities are the volume and circumference of the excursion set. These three measures can be placed in the wider framework of Minkowski functionals by natural mathematical considerations (Mecke, Buchert & Wagner 1994) and have found a wide application in the analysis of CMB maps (e.g. Smoot et al. 1994; Kogut et al. 1996; Schmalzing & G orski 1998; Shandarin et al. 2002).

The multifractal formalism has been applied to CMB maps by Pompillo et al. (1995) and Diego et al. (1999). The multifractal formalism, however, is not the only method derived from nonlinear sciences which can successfully be applied to CMB investigations. Being aware that it is often very difficult to doubtlessly identify (multi-)fractal dimensions for a limited number of points, the method of surrogates (Theiler et al. 1992, for a review see Schreiber & Schmitz 2000) has been established in the last years in order to detect (weak) nonlinearities in time series. The basic idea is to compute nonlinear statistical measures for the original data set and of an ensemble of surrogate data sets, which mimic the linear properties of the original data set. If the computed measure for the original data is significantly different from the values obtained for the surrogate sets, one can infer that the data were generated by a nonlinear process.

Several approaches for the generation of surrogates have been established depending on the data and on the constraints to be preserved. Some algorithms make explicit use of Fourier transformations like the amplitude adjusted Fourier transform algorithm (AAFT) (Theiler et al. 1992) and the iterative amplitude adjusted Fourier transform algorithm (ITAAFT) (Schreiber & Schmitz 1996). Other approaches use simulated annealing techniques, where the constraints are implemented as a suitable cost function, which is to be minimized (Schreiber 1998).

So far, these methods have only been applied to time series analysis, although the general approach is not restricted to time series analysis. Recently it has been demonstrated (R ath et al. 2002) in the large scale structure analysis that surrogates can successfully be generated for three-dimensional point distributions, for which it is known that they have nonlinear correlations. It has further been shown that statistical measures which estimate the local scaling properties of the point set are well suited to account for the nonlinearities in the data.

In this paper we show the feasibility to generate surrogates, which mimic the power spectrum and the amplitude distribution, for CMB maps using a two-dimensional version of the well-known ITAAFT approach. As statistical measures for testing for non-Gaussian signatures in the maps we use weighted scaling indices as well as Minkowski functionals. The results of our studies are compared with those obtained with established methods. In this study we are only interested in a relative comparison between the different techniques for testing for non-Gaussian signatures. Therefore we do not consider effects of cosmic variance because they were also not taken into account in the studies we compare our results with.

The outline of the paper is as follows. Section 2 reviews in some details the method to generate surrogates for the two-

dimensional case. In Section 3 we introduce as test statistics weighted scaling indices and the Minkowski functionals. The results of applying our method to simulated CMB maps are shown in Section 4. Finally, we present our conclusions and give an outlook on future studies in Section 5.

## 2 SURROGATES

An iteration scheme is used to generate surrogate data which have the same power spectrum and the same temperature distribution. As a brief review and to introduce the notations we describe the extension of the algorithm for the two-dimensional case of CMB temperature maps. Assume a two-dimensional pixelized field of random fluctuations in the CMB brightness temperature  $T(x, y) = T(\vec{r})$ ,  $x, y = 1, \dots, N$ .

Before the iteration starts two quantities have to be calculated:

- 1) A copy  $\eta(\vec{r}) = \text{rank}(T(\vec{r}))$  of the original temperature values, which is sorted by magnitude in ascending order, is computed.
- 2) The absolute values of the amplitudes of the discrete Fourier transform  $T(\vec{k})$  of  $T(\vec{r})$ ,

$$|T(\vec{k})| = \left| \frac{1}{N^2} \sum_{x,y} T(\vec{r}) e^{-2\pi i \vec{k} \cdot \vec{r} / N} \right| \quad (1)$$

are calculated as well.

The starting point for the iteration is a random shuffle  $T_0(\vec{r})$  of the data. Each iteration consists of two consecutive calculations:

First,  $T_0(\vec{r})$  is brought to the desired sample power spectrum. This is achieved by using a crude 'filter' in the Fourier domain: The Fourier amplitudes are simply *replaced* by the desired ones.

For this the Fourier transform of  $T_n(\vec{r})$  is taken:

$$T_n(\vec{k}) = \frac{1}{N^2} \sum_{x,y} T_n(\vec{r}) e^{-2\pi i \vec{k} \cdot \vec{r} / N} . \quad (2)$$

In the inverse Fourier transformation the actual amplitudes are replaced by the desired ones and the phases defined by  $\tan \psi_n(\vec{k}) = \text{Im}(T_n(\vec{k})) / \text{Re}(T_n(\vec{k}))$  are kept:

$$s(\vec{r}) = \frac{1}{N^2} \sum_{k_x, k_y} e^{i\psi_n(\vec{k})} |T(\vec{k})| e^{-2\pi i \vec{k} \cdot \vec{r} / N} . \quad (3)$$

Thus this step enforces the correct power spectrum, but usually the distribution of the amplitudes in the CMB image will be modified.

Second, a rank ordering of the resulting data set  $s(\vec{r})$  is performed in order to adjust the spectrum of amplitudes. The intensities  $T_{n+1}(\vec{r})$  are obtained by replacing the values of  $s(\vec{r})$  with those stored in  $\eta(\vec{r})$  according to their rank:

$$T_{n+1}(\vec{r}) = \eta(\text{rank}(s(\vec{r}))) . \quad (4)$$

It can heuristically be understood that the iteration scheme is attracted to a fixed point (for an explanation see e.g. Schreiber & Schmitz 2000). The final accuracy that can be reached depends on the size and properties of the data sets but is generally sufficient for hypothesis testing.

### 3 TEST STATISTICS

#### 3.1 Weighted scaling indices and their local means

We use weighted scaling indices (Räth et al. 2002) for the estimation of *local* scaling properties of a point set and apply this method in order to characterize different structural features of the spatial patterns in the images. Consider a temperature map  $T(x, y)$  of size  $M_1 \times M_2$ . Each pixel is assigned with a temperature value  $T(x, y)$  thus containing both space and temperature information that can be encompassed in a three-dimensional vector  $\vec{p} = (x, y, T(x, y))$ . The CMB image can now be regarded as a set of  $N$  points  $P = \{\vec{p}_i\}, i = 1, \dots, N, N = |M_1 \times M_2|$ . For each point the local weighted cumulative point distribution  $\rho$  is calculated. In general form this can be written as

$$\rho(\vec{p}_i, r) = \sum_{j=1}^N s_r(d(\vec{p}_i, \vec{p}_j)), \quad (5)$$

where  $s_r(\bullet)$  denotes a kernel function depending on the scale parameter  $r$  and  $d(\bullet)$  a distance measure.

The weighted scaling indices  $\alpha(\vec{p}_i, r)$  are obtained by calculating the logarithmic derivative of  $\rho(\vec{p}_i, r)$  with respect to  $r$ ,

$$\alpha(\vec{p}_i, r) = \frac{\partial \log \rho(\vec{p}_i, r)}{\partial \log r} = \frac{r}{\rho} \frac{\partial}{\partial r} \rho(\vec{p}_i, r). \quad (6)$$

In principle any differentiable kernel function and any distance measure can be used for calculating  $\alpha$ . In the following we use the Euclidean norm as distance measure and a set of Gaussian shaping function. So the expression for  $\rho$  simplifies to

$$\rho(\vec{p}_i, r) = \sum_{j=1}^N e^{-\left(\frac{d_{ij}}{r}\right)^q}, d_{ij} = \|\vec{p}_i - \vec{p}_j\|. \quad (7)$$

The exponent  $q$  controls the weighting of the points according to their distance to the point for which  $\alpha$  is calculated. In this study we calculate  $\alpha$  for the case  $q = 2$ . Using the definition in (6) yields for the weighted scaling indices

$$\alpha(\vec{p}_i, r) = \frac{\sum_{j=1}^N q \left(\frac{d_{ij}}{r}\right)^{q-1} e^{-\left(\frac{d_{ij}}{r}\right)^q}}{\sum_{j=1}^N e^{-\left(\frac{d_{ij}}{r}\right)^q}}. \quad (8)$$

Structural components of the temperature map are characterized by the calculated value of  $\alpha$  of the pixels belonging to them. For example, points in a point-like structure have  $\alpha \approx 0$  and pixels forming line-like structures have  $\alpha \approx 1$ . Area-like structures are characterized by  $\alpha \approx 2$  of the pixels belonging to them. A uniform distribution of points yields  $\alpha \approx 3$  which is equal to the dimension of the configuration space. Pixels in the vicinity of point-like structures, lines or areas have  $\alpha > 3$ .

The scaling indices for the whole random field under study form the frequency distribution  $N(\alpha)$

$$N(\alpha)d\alpha = \#(\alpha \in [\alpha, \alpha + d\alpha]) \quad (9)$$

or equivalently the probability distribution

$$P(\alpha)d\alpha = \text{Prob}(\alpha \in [\alpha, \alpha + d\alpha]) \quad (10)$$

This representation of the temperature map can be regarded as a structural decomposition of the image where the

pixels are differentiated according to the local morphological features of the structure elements to which they belong to.

On the other hand, the weighted scaling indices can be regarded as a filter response of a local nonlinear filter acting in the CMB image. The findings in the field of the perception and analysis image patterns and image textures (for a review see Julesz 1991) suggest that, when two textures  $T_1$  and  $T_2$  are discriminable, they are distinguished by different spatial averages of some locally computed nonlinear response function  $R$ . Based on these considerations we calculate the local mean values  $\langle \alpha \rangle$  for the scaling indices in a sliding window of size  $K$ ,

$$\langle \alpha(x_i, y_i) \rangle = \frac{1}{K} \sum_{x,y} \alpha(x_i, y_i) \Theta\left(\frac{K}{2} - |x_i - x|\right) \Theta\left(\frac{K}{2} - |y_i - y|\right), \quad (11)$$

for all pixels and analyse the respective probability distribution

$$P(\langle \alpha \rangle)d\alpha = \text{Prob}(\langle \alpha \rangle \in [\langle \alpha \rangle, \langle \alpha \rangle + d\langle \alpha \rangle]). \quad (12)$$

In all following calculation we use a window size of  $K = 20$ .

#### 3.2 Minkowski functionals

Minkowski functionals incorporate correlation functions of higher orders and supply global morphological information about structures under study. It has been shown that the  $d + 1$  Minkowski functionals provide a unique description of the global morphology of a  $d$ -dimensional pattern. In our two-dimensional temperature maps we have three Minkowski functionals, which can be interpreted as area ( $M_0$ ), circumference ( $M_1$ ) and Euler characteristic ( $M_3$ ) of an excursion set  $R(\nu)$ :

$$M_0(\nu) = \int_{R(\nu)} dS, \quad (13)$$

$$M_1(\nu) = \int_{\partial R(\nu)} dl, \quad (14)$$

$$M_2(\nu) = \int_{\partial R(\nu)} \frac{dl}{r}. \quad (15)$$

$\partial R(\nu)$  is the boundary of the excursion region  $R(\nu)$  at the threshold temperature  $\nu$ . The differentials  $dS$  and  $dl$  denote the elements of area and of length along the boundary, and  $r$  is the radius of the curvature of the boundary. The excursion set is taken as the region of the CMB map above a certain threshold  $\nu$ . The Minkowski functionals are therefore functions of the threshold temperature  $\nu$ . We estimate the Minkowski functionals for pixelized temperature maps in flat space, which is sufficient for our comparisons of two-dimensional random fields desired in this paper. The calculation of the surface area and circumference of the excursion sets in a pixelized map is straightforward. The Euler characteristic is determined by looking at the angle deficits of the vertices as described in Mecke (1996). In our study, where we want to compare the original maps with their surrogates with equal temperature distribution, the Minkowski functional  $M_0$  will - by definition - be equal for the original and surrogate data and will therefore have no discriminative power. Thus we will only calculate and further analyse  $M_1$  and  $M_2$ .

#### 4 APPLICATION TO SIMULATED CMB MAPS

We apply the method of surrogates and weighted scaling indices to a simulated non-Gaussian CMB map, which is a realization of  $12.8 \text{ deg}^2$  CMB anisotropies due to the Kayser-Stebbin effect from cosmic strings (e.g. Bouchet, Bennett & Stebbins 1988). Topological defects, although not the main source of cosmic structure, are predicted in many particle physics models and are thought to be responsible for the formation of cosmic strings at the end of an inflationary period. Fig. 1 (lower left image) shows a CMB anisotropy map generated by cosmic strings seen after last scattering corresponding to secondary anisotropies imprinted via the moving lens effect. Each infinitesimal element of the cosmic string acts as a source of 'butterfly'-pattern whose superpositions lead to step-like discontinuities along the string with a magnitude proportional to the local string velocity transversal to the line of sight (LOS). Therefore non-Gaussianities are induced by the step-like discontinuities.

We will test for non-Gaussianity by generating 20 surrogate maps for the original non-Gaussian map and for maps with additive white Gaussian noise with five different fluctuation levels. The noise levels are chosen with *rms* ratio  $SNR = 8, 4, 2, 1$  and  $0.5$ . In Fig. 2 the convergence of the algorithm as a function of the iteration steps is shown. We therefore calculated the relative deviation  $\Delta I_{\text{Fourier}}$  of the power spectrum at the  $n$ -th iteration step from the original power spectrum,

$$\Delta I_{\text{Fourier}} = \frac{\sum_{k_x, k_y} (|I_n(k_x, k_y)| - |I(k_x, k_y)|)^2}{\sum_{k_x, k_y} |I(k_x, k_y)|^2}. \quad (16)$$

One can clearly see that the algorithm converges quickly, reproduces the original power spectrum with a very high accuracy and saturates after approximately 30 iteration steps. In the following all surrogates are generated using 100 iteration steps.

In order to test for the Gaussianity of the obtained surrogate maps we analysed the probability density of the Fourier phases  $P(\phi)$ . Therefore we calculated the deviations  $\Delta P(\phi)$ ,

$$\Delta P(\phi) = \frac{P_{\text{surrogate}}(\phi) - \langle P_{\text{random}}(\phi) \rangle}{\sigma_{P_{\text{random}}(\phi)}}, \quad (17)$$

of the surrogate maps from the probability densities  $P_{\text{random}}(\phi)$  of a random phase distribution. The mean  $\langle P_{\text{random}}(\phi) \rangle$  and the standard deviation  $\sigma_{P_{\text{random}}(\phi)}$  were derived from 100 realizations of random phase distributions. Fig. 3 shows as an example the deviations  $\Delta P(\phi)$  for the case  $SNR = 2$ . For most of the bins  $\Delta P(\phi)$  is below the  $1\sigma$ -level. Only for a few uncorrelated bins the deviation becomes larger (smaller) than 2 ( $-2$ ). Therefore, no statistically significant deviations from a random distribution are found. It should be noted that we did the same analysis for all other noise levels and obtained the same results.

In Fig. 1 the original (noisy) images and two respective surrogates are displayed. One might observe that the surrogate maps have 'more granular' structures but the differences between the original and surrogate maps are not very pronounced, especially when the noise level is increased. In order to quantify the structures in the images we calculate the spectrum of weighted scaling indices for all

maps. We normalized the temperature distribution so that the standard deviation  $\sigma_T$  is four at each fluctuation level. (Other normalizations are conceivable.) The radius for the calculation of the weighted scaling indices  $\alpha$  is chosen to  $r = 1.5, 2, 3, 5$  and  $6$  pixels. The original size of the images and their surrogates is  $256 \times 256$  pixels. In order to avoid edge effects we analyse only the inner part ( $216 \times 216$  pixels) of the  $\alpha$ - and  $\langle \alpha \rangle$ -images further. Likewise, we calculate the Minkowski functionals only for the inner part of the images.

We start the analysis of the weighted scaling indices by plotting the global means  $\langle \alpha \rangle_{\text{global}}$  as a function of the different radii (Fig. 4) for the original map and the respective surrogates. Recall that the differences between non-Gaussianity and Gaussianity is reflected in the differences between the test statistics applied to the original data and the surrogate data. The scatter of the surrogates leads to measures of the statistical significance of the deviation between non-Gaussianity and Gaussianity. In the undisturbed case (Fig. 4 (a)) one finds that  $\langle \alpha \rangle_{\text{global}}$  for the original map is simply shifted to lower values for all radii. This shift is due to the more 'granular-like' structure on small scales in the surrogates. But for all images the global mean of the scaling indices does not change very much when the radius is increased. Therefore, a very good discrimination between the two classes of maps (original and surrogates) is possible for all radii. For the noisy images (Fig. 4 (b) - (f)) one finds larger variations with varying radius and the original map is only clearly discriminable from the surrogates until a noise level of  $SNR = 2$  (Fig. 4 d).

In Fig. 5 the global standard deviation  $\sigma_\alpha$  of the scaling indices as a function of the different radii are shown for the original map and the respective surrogates. For this global quantity one can essentially find that for noise levels up to  $SNR = 1$  (Fig. 5 e) one can find length scales  $r$  at which a discrimination between the original and surrogates is possible.

Similar discrimination results can also be obtained by calculating the global standard deviation  $\sigma_{\langle \alpha \rangle}$  of the local means  $\langle \alpha \rangle$  (Fig. 6). For this quantity it is remarkable that one finds for all noise levels very different functional behavior for the surrogates compared to the original maps. So it is very likely that refined analyses of the slopes and/or the curvatures of  $\sigma_{\langle \alpha \rangle}(r)$  will yield very good discrimination results.

We proceed further with a differential analyses of the scaling indices and therefore concentrate on the probability densities  $P(\alpha)$  for the (noisy) maps and their 20 surrogates for one value of  $r$  ( $r = 5$ ) (see Fig. 7). It can clearly be seen that in the undisturbed case the differences between the surrogates and the original map in the  $P(\alpha)$  spectrum are very significant, whereas the spectral differences in the noisy cases are not so evident in this representation. In order to quantify the observed differences in the measured probability densities  $P(\alpha)$  (and  $P(\langle \alpha \rangle)$  see below) we calculate the deviation  $\Delta P(\alpha)$ ,

$$\Delta P(\alpha) = \frac{P_{\text{original}}(\alpha) - \langle P_{\text{surrogate}}(\alpha) \rangle}{\sigma_{P_{\text{surrogate}}(\alpha)}}, \quad (18)$$

of the  $P(\alpha)$  spectrum of the original data from the mean spectrum as derived from the respective surrogates normalized to their standard deviation. Fig. 8 shows  $\Delta P(\alpha)$

for all noise levels. We obtain deviations of more than  $3\sigma$  up to a noise level of  $SNR = 1$ . In Fig. 9 and Fig. 10 the probability density  $P(\langle \alpha \rangle)$  and deviation  $\Delta P(\langle \alpha \rangle)$  for the local means of the scaling indices  $\langle \alpha \rangle$  are displayed. Using this quantity the differences between the surrogates and the original maps become even more significant. The probability distributions in the noisy cases are broader for the surrogates (compare also Fig. 6) and shifted to higher values (no noise) or to lower values (high noise level). Consequently we obtain for all noise levels systematic deviations  $\Delta P(\langle \alpha \rangle)$ , which have maxima for their absolute value, which are at least larger than  $1.5\sigma$  for the respective  $\langle \alpha \rangle$ . Thus a discrimination between original and surrogate maps seems possible up to noise levels of  $SNR = 0.5$ .

We now compare these results with more standard morphological analyses of temperature maps, which are based on Minkowski functionals. Fig. 11 shows the circumference  $M_1$  and Fig. 12 the Euler characteristic  $M_2$  for all noise levels and for the original and surrogate maps. In both cases the Minkowski functionals for the original map differ significantly from that for the surrogate maps up to a noise level of  $SNR = 1$ . For the Euler characteristic  $M_2$  we can also observe that there are slight systematic difference between the original and surrogate maps in the case of  $SNR = 0.5$ . These results are very remarkable if they are compared with those obtained by Chiang, Naselsky & Coles (2002). In their study they calculate Minkowski functionals for the same CMB map and for maps with the same power spectrum but random phases. The authors find that an identification of non-Gaussian signatures is only possible at most up to  $SNR = 2$ . In our case where both the power spectrum and the amplitude distribution is kept one can clearly distinguish between the original map and the surrogates even at much higher noise levels using Minkowski functionals. Thus we can reject the hypothesis that the CMB map is Gaussian with same power spectrum and same intensity distribution and therefore clearly identify non-Gaussianity at high noise levels. The additional constraint of keeping the amplitude distribution leads to smaller fluctuations of the Minkowski functionals for the Gaussian surrogate maps. Therefore, a more sensitive discrimination between maps with and without non-Gaussian signatures is possible.

## 5 CONCLUSIONS

We have shown that it is possible to generate surrogate CMB maps which mimic both the power spectrum *and* the amplitude distribution of the original simulated map by applying the method of iteratively refined surrogates.

As statistical measures being sensitive to non-Gaussianity we calculated weighted scaling indices and Minkowski functionals for the original and surrogate maps. For both measures the values for the original data are significantly different from the values obtained for the surrogate sets. Therefore a clear evidence for the non-Gaussian signatures in the maps is given. We further tested the robustness of our approach with respect to white Gaussian (pixel) noise and found that a detection of the non-Gaussianity up to SNR-

ratio of 0.5 is made possible. This result applies to both test statistics.

Comparing these results with those obtained with other techniques (e.g. phase mapping) as proposed by Chiang, Naselsky & Coles (2002) we find that our approach is superior concerning robustness with respect to noise. Due to the refined construction of the surrogate maps we were able to detect non-Gaussian signatures using Minkowski functionals at higher noise levels as in the above mentioned work.

So both methods the construction of amplitude adjusted surrogates and the weighted scaling indices as an estimator for local scaling properties in image data turned out to be of great usefulness in the detection of non-Gaussianity in CMB-maps. Thus we obtained very promising first results by applying new approaches derived from nonlinear sciences to CMB map analysis.

It is likely that a more sophisticated analysis of the scaling indices will even increase the statistical significance of the discrimination results. So the improvement of the methods proposed in this study and their application to more realistic simulated CMB maps incorporating mixture models as well as to real data obtained with the WMAP- and Planck-satellites will be a rich field for future studies.

## ACKNOWLEDGMENTS

The authors want to thank Milenko Zuzic and Michael Kretschmer for giving us the opportunity to discuss cosmological questions in a relaxed atmosphere.

## REFERENCES

- Albrecht A., Steinhardt P.J., 1982, PRL, 48, 1220
- Barreiro R.B., Hobson M.P., 2001, MNRAS, 327, 813
- Bernardeau F., Uzan J.-P., 2002, astro-ph/0209330
- Bouchet F.R., Bennett D.P., Stebbins A., Nature, 1988, 335, 410
- Cayón L., Sanz J.L., Martínez-González E., Argüeso F., Gallegos J.E., Górski K.M., Hinshaw G., 2001, MNRAS, 326, 1243
- Coles P., 1988, MNRAS, 234, 509
- Coles P., Barrow J. D., 1987, MNRAS, 228, 407
- Chiang L.-Y., Coles P., Naselsky P., 2002, astro-ph/0207584
- Chiang L.-Y., Naselsky P., Coles P., 2002, astro-ph/0208235
- Diego J.M., Martínez-González E., Sanz J.L., Mollerach S., Martínez V.J., 1999, MNRAS, 306, 427
- Guth A. H., 1981, PRD, 23, 347
- Hobson M.P., Jones A.W., Lasenby A.N., 1999, MNRAS, 309, 125
- Hu W., 2001, PRD, 64, 083005
- Julesz B., 1991, Rev. Mod. Phys., 63, 735
- Kogut A., Banday A.J., Bennett C.L., Górski K.M., Hinshaw G., Smoot G.F., Wright E.L., 1996, ApJ, 464, L29
- Linde, A.D., 1982, Phys. Lett. B, 108, 389
- Mataresse S., Verde L., Heavens A.F., 1997, 290, 651
- Mecke K., 1996, PRE, 53, 4794
- Mecke K., Buchert T., Wagner H., 1994, A & A, 288, 697
- Pompilio M.P., Bouchet F.R., Murante G., Provenzale A., 1995, ApJ, 449, 1
- Räth C., Bunk W., Huber M., Morfill G., Retzlaff J., Schuecker P., 2002, MNRAS, in press (astro-ph/0207140)
- Sandvik H.B., Magueijo J., 2001, MNRAS, 325, 463
- Schmalzing J., Gorski K.M., 1998, MNRAS, 297, 355
- Schreiber T., 1998, PRL, 80, 2105

6 *C. Räth and P. Schuecker*

- Schreiber T., Schmitz A., 1996, PRL, 77, 635  
Schreiber T., Schmitz A., 2000, Physica D, 142, 346  
Shandarin S.F., Feldman H.A., Xu Y., Tegmark M., 2002, ApJS, 141, 1  
Smoot G.F., Tenorio L., Banday A.J., Kogut A., Wright E.L., Hinshaw G., Bennett C.L., 1994, ApJ, 437, 1  
Steinhardt P. J., Turok N., 2002, astro-ph/0204479  
Theiler J., Eubank S., Longtin A., Galdrikian B., Farmer J.D., 1992, Physica D, 58, 77  
Turok N., 1996, ApJ, 473, L5  
Verde L., Wang L., Heavens A.F., Kamionkowski M., 2000, MNRAS, 313, 141  
Verde L., Heavens A.F., 2001, ApJ, 553, 14

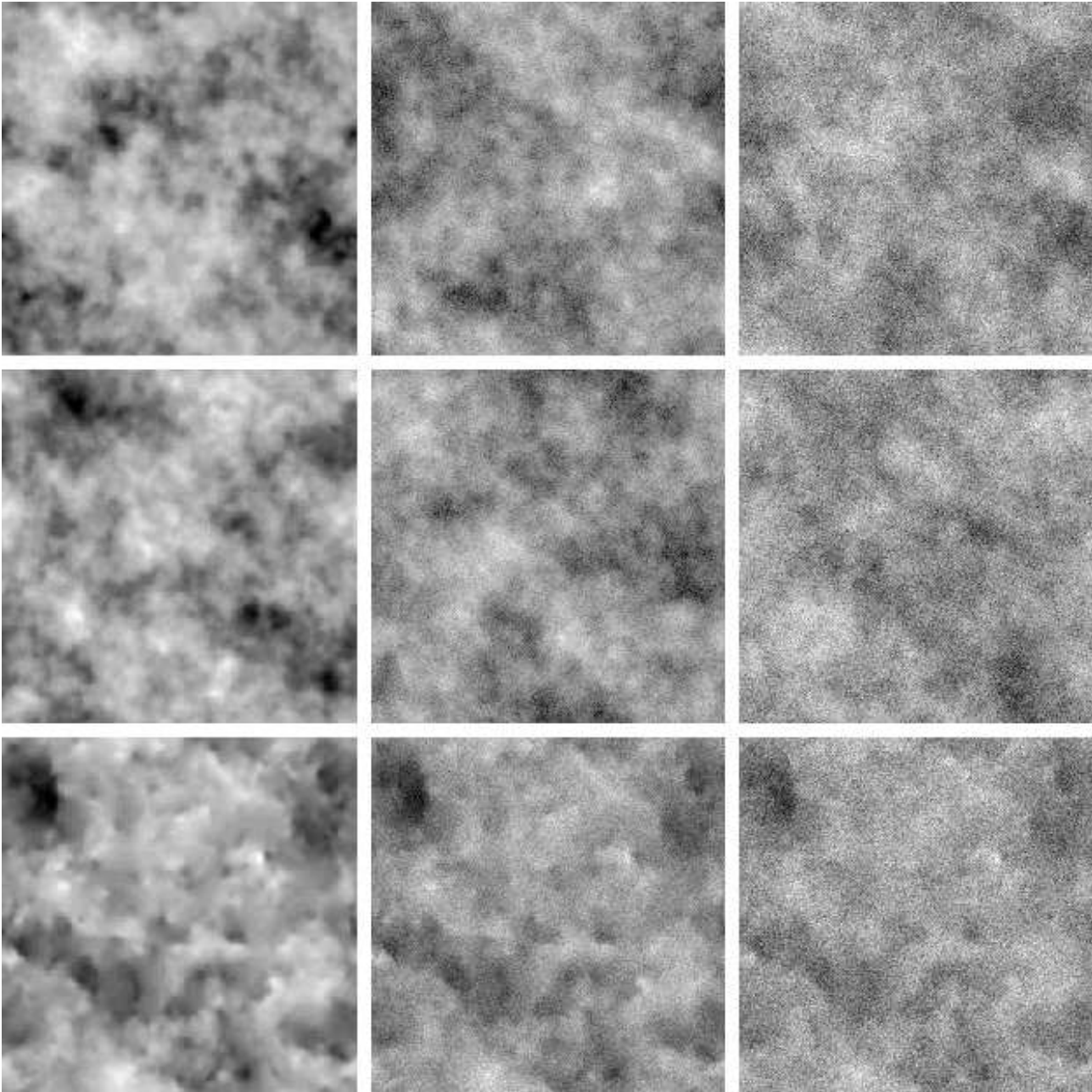


**Figure 1.** Lowest row: Temperature map  $T(x, y)$ ,  $T \in [-100, 100]\mu K$ , without additive noise (left image). Some step-like discontinuities inducing non-Gaussianity are quite apparent. Temperature maps with additive noise: SNR = 2 (middle) and SNR = 1 (right). Upper rows: Two respective surrogate images.

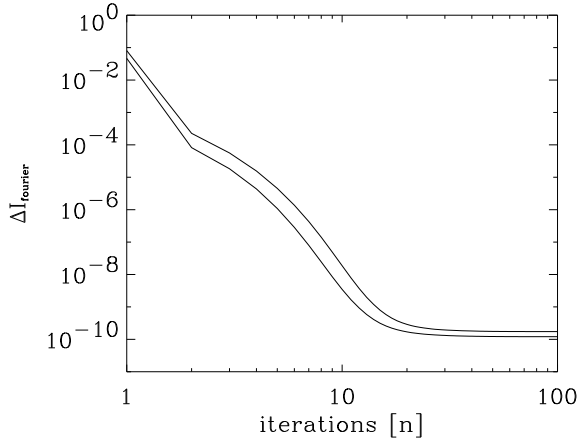


**Figure 2.** Convergence of the iteration scheme for two noisy CMB maps with  $SNR = 4$  (upper curve) and  $SNR=2$  (lower curve).

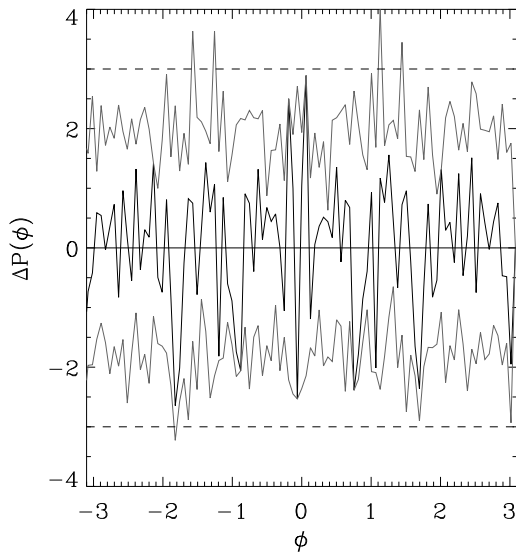


**Figure 3.** Deviation  $\Delta P(\phi)$  of the probability density of the Fourier phases for one surrogate ( $SNR = 4$ ). The grey lines indicate the maximal (minimal) deviations for each bin as derived from the 20 surrogates generated for this noise level.



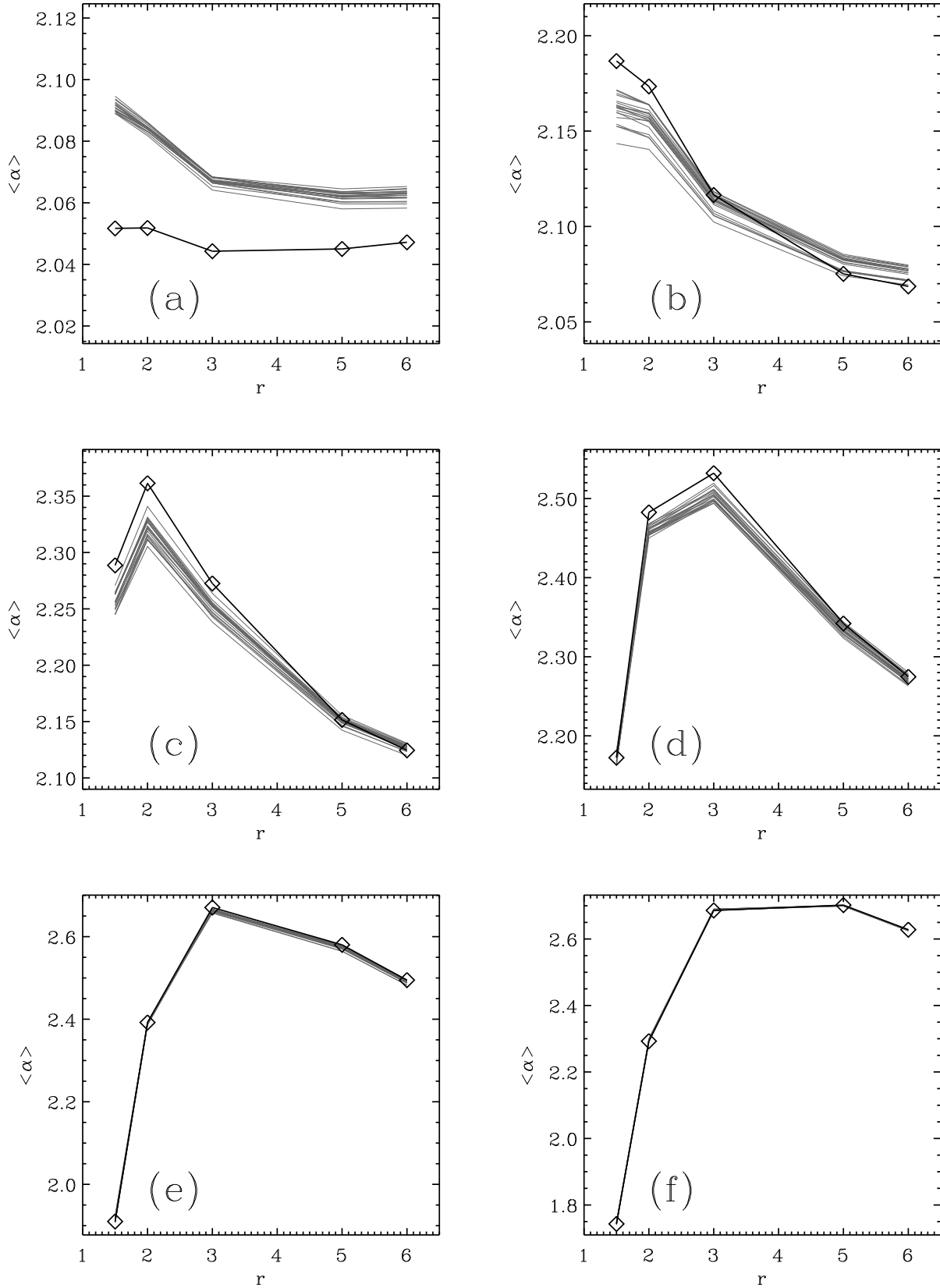


**Figure 4.** Global mean values  $\langle \alpha \rangle_{global}$  as a function of  $r$  for the original image (black) and for the surrogates (gray). Panel (a) is for the pure temperature map. Panel (b), (c), (d), (e) and (f) are the graphs for the combined map of CMB and additive white gaussian noise with SNR = 8, 4, 2, 1 and 0.5, respectively.

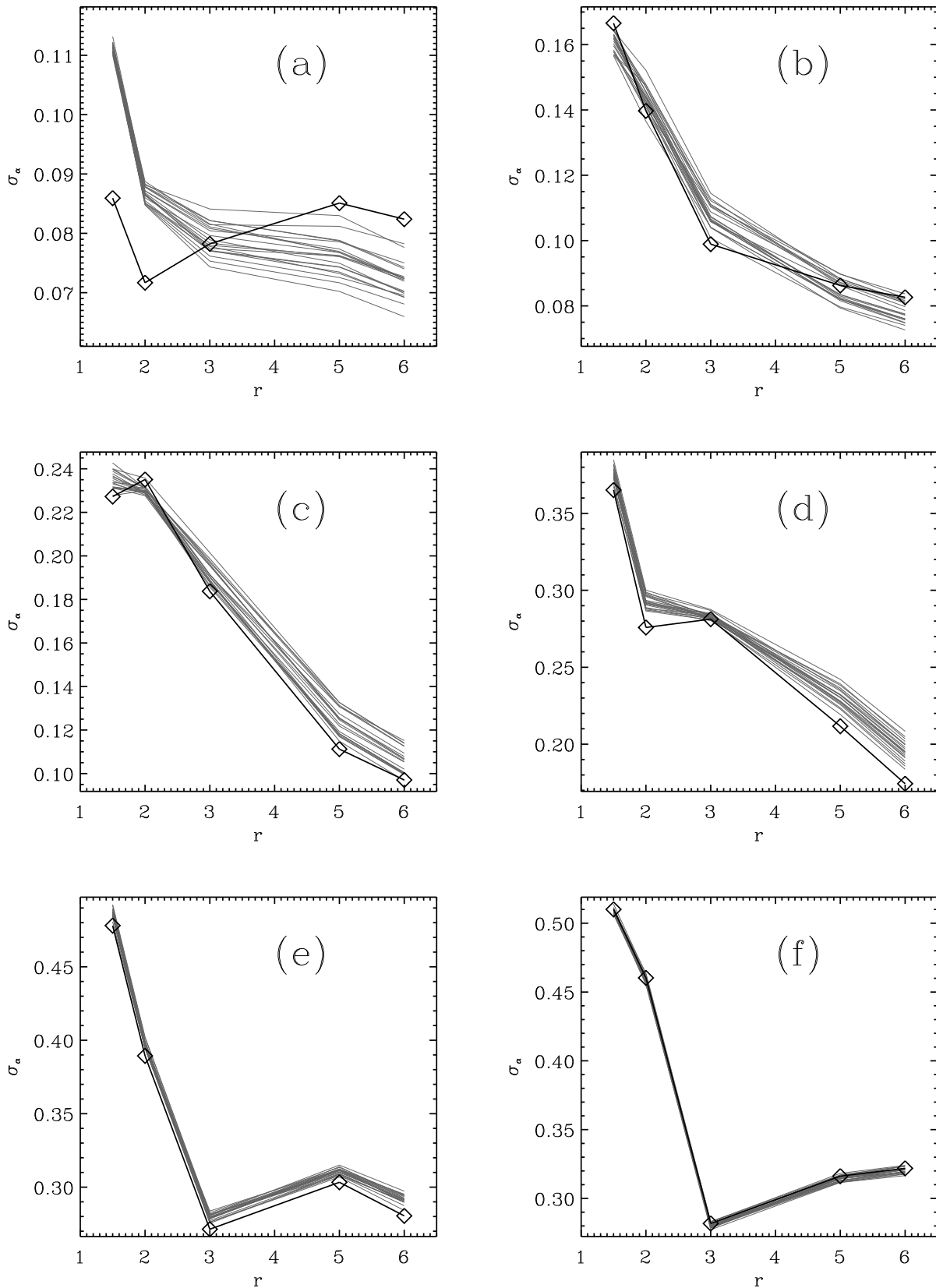


**Figure 5.** Global standard deviation  $\sigma_\alpha$  as a function of  $r$  for the original image (black) and for the surrogates (gray). Panel (a) is for the pure temperature map. Panel (b), (c), (d), (e) and (f) are the graphs for the combined map of CMB and additive white gaussian noise with SNR = 8, 4, 2, 1 and 0.5, respectively.

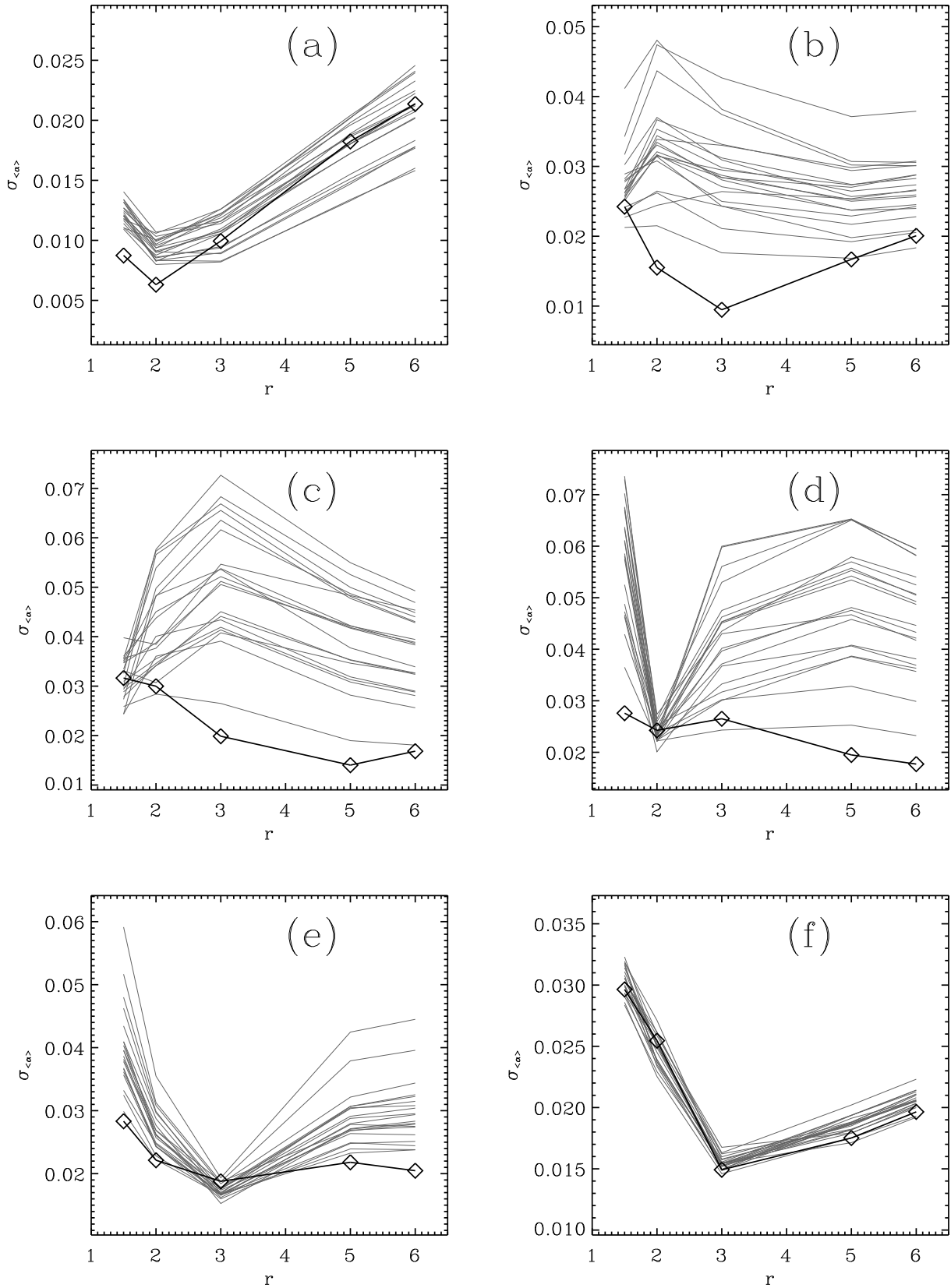


**Figure 6.** Global standard deviation  $\sigma_{\langle\alpha\rangle}$  as a function of  $r$  for the original image (black) and for the surrogates (gray). Panel (a) is for the pure temperature map. Panel (b), (c), (d), (e) and (f) are the graphs for the combined map of CMB and additive white gaussian noise with SNR = 8, 4, 2, 1 and 0.5, respectively.

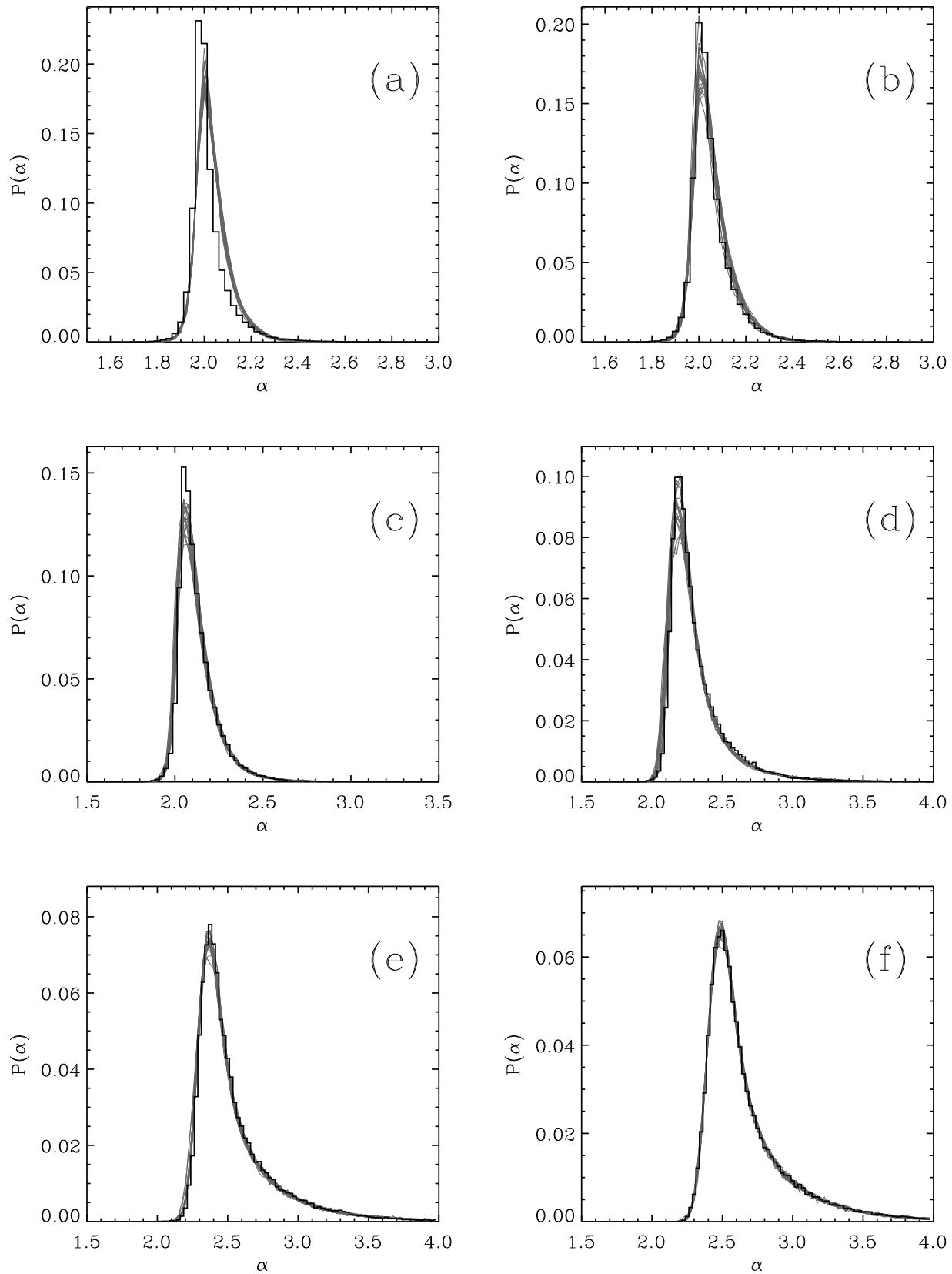


**Figure 7.** Probability distribution  $P(\alpha)$  for  $r = 5$  for the original (black) and surrogates (gray). Panel (a) is for the pure temperature map. Panel (b), (c), (d), (e) and (f) are the graphs for the combined map of CMB and additive white gaussian noise with SNR = 8, 4, 2, 1 and 0.5, respectively.

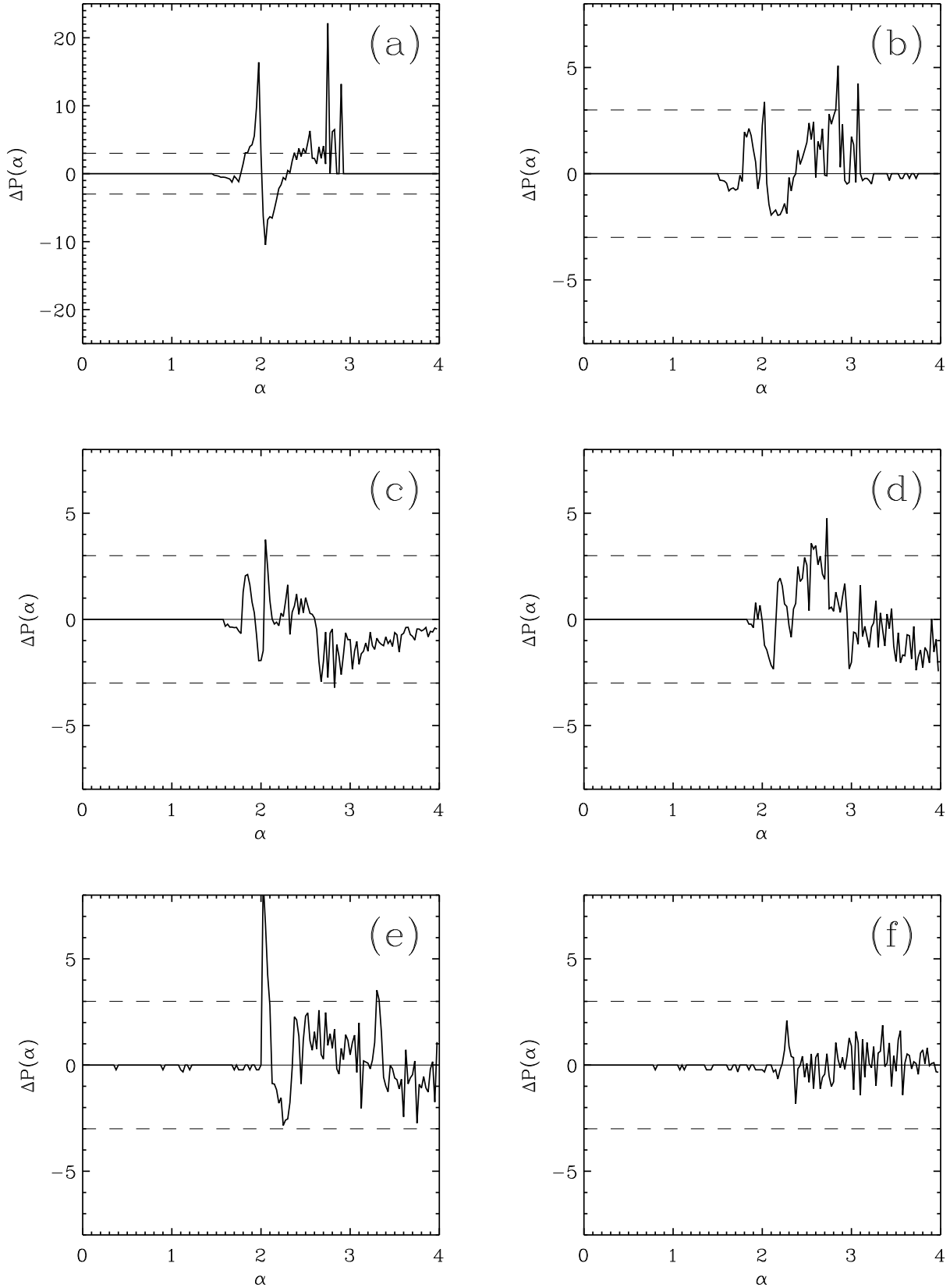


**Figure 8.** Deviation  $\Delta P(\alpha)$  of the original image from the mean surrogate distribution. Panel (a) is for the pure temperature map. Panel (b), (c), (d), (e) and (f) are the graphs for the combined map of CMB and additive white gaussian noise with SNR = 8, 4, 2, 1 and 0.5, respectively.

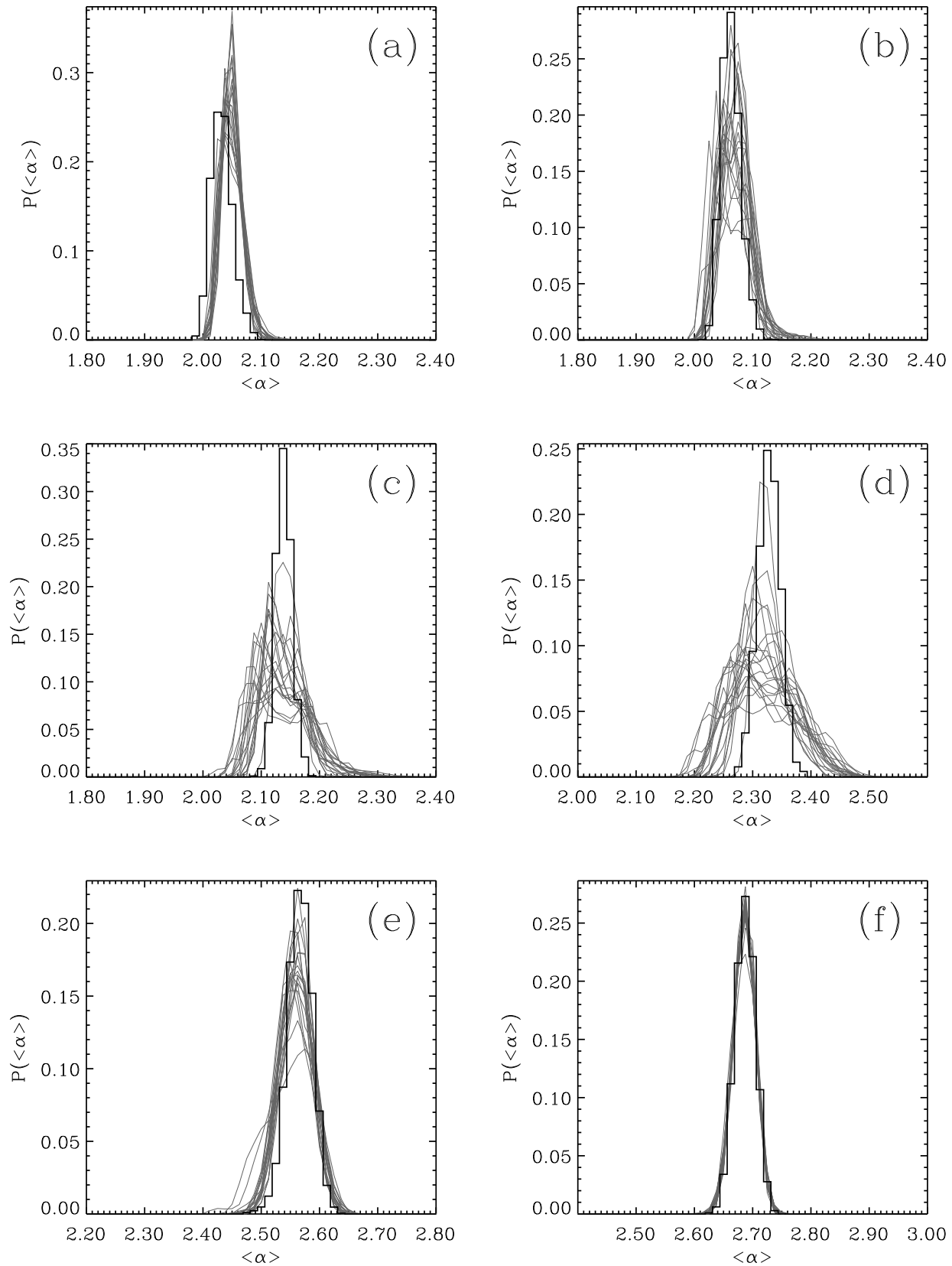


**Figure 9.** Probability distribution  $P(\langle \alpha \rangle)$  for  $r = 5$  for the original (black) and surrogates (gray). Panel (a) is for the pure temperature map. Panel (b), (c), (d), (e) and (f) are the graphs for the combined map of CMB and additive white gaussian noise with SNR = 8, 4, 2, 1 and 0.5, respectively.

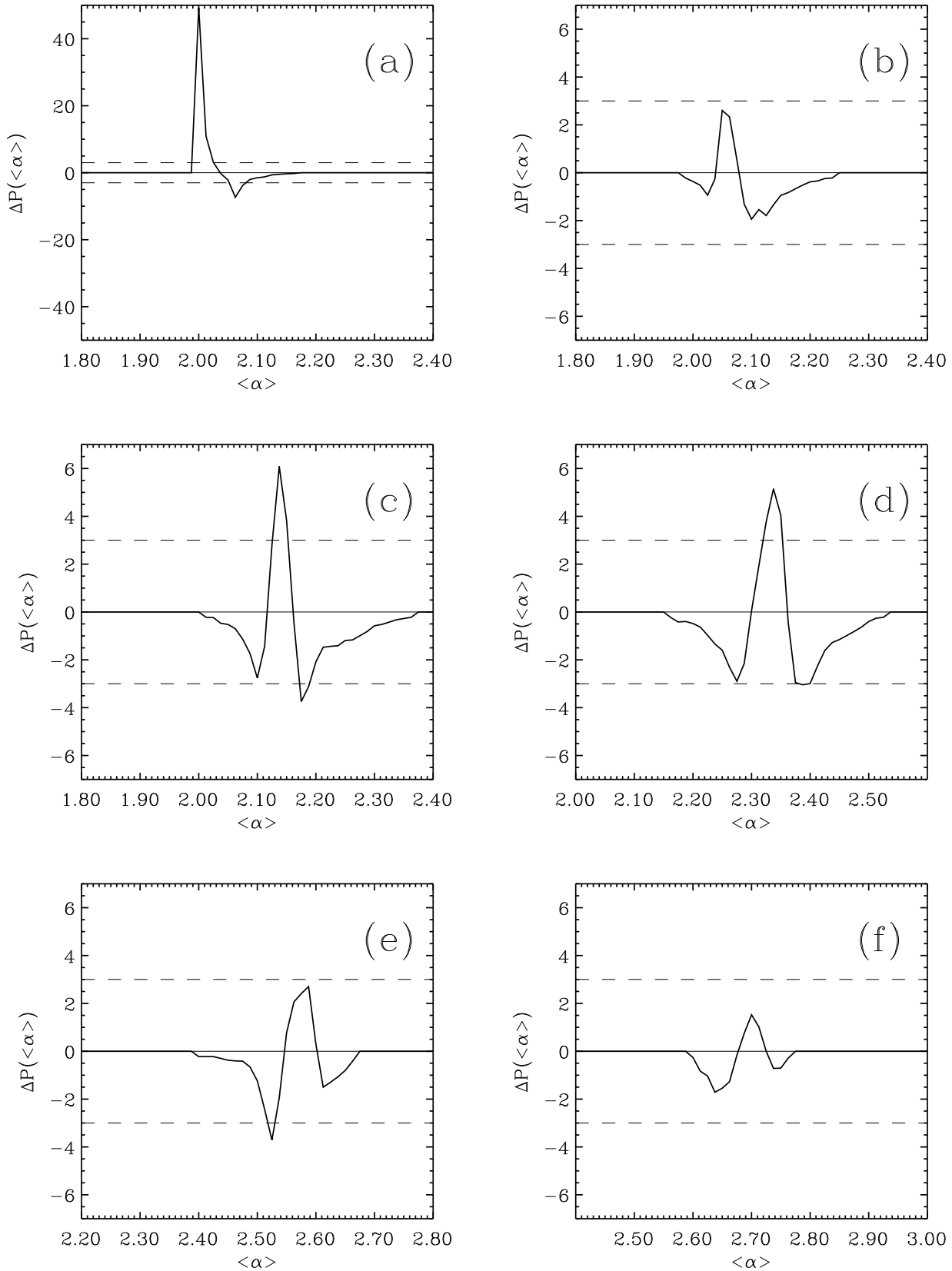


**Figure 10.** Deviation  $\Delta P(\langle \alpha \rangle)$  of the original image from the mean surrogate distribution. Panel (a) is for the pure temperature map. Panel (b), (c), (d), (e) and (f) are the graphs for the combined map of CMB and additive white gaussian noise with SNR = 8, 4, 2, 1 and 0.5, respectively.

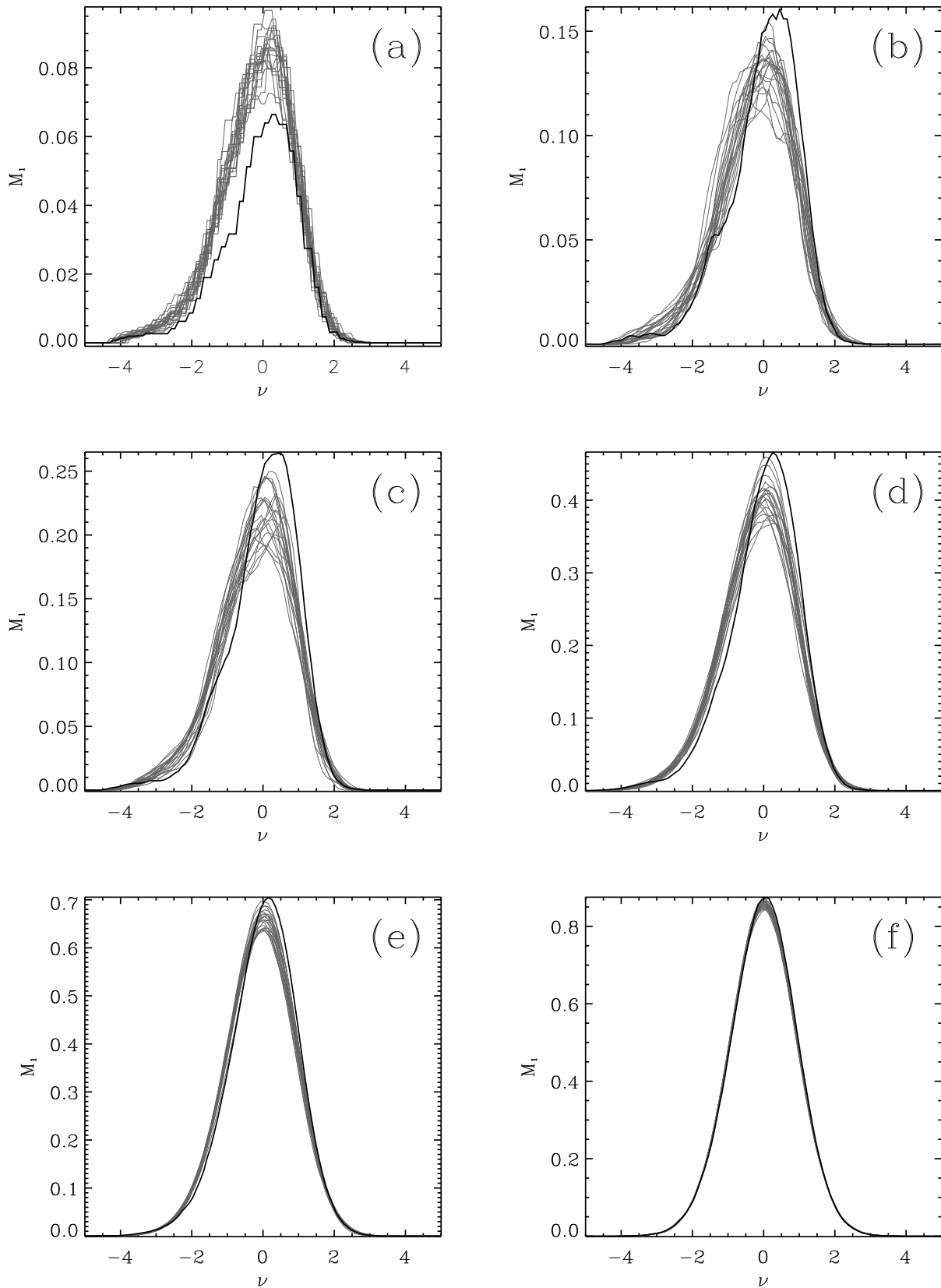


**Figure 11.** Minkowski functional  $M_1$  of the original image and the surrogates. The map intensities are normalized to have zero mean and a standard deviation of one. The thresholds  $\nu$  are in units of the standard deviation. Panel (a) is for the pure temperature map. Panel (b), (c), (d), (e) and (f) are the graphs for the combined map of CMB and additive white gaussian noise with  $\text{SNR} = 8, 4, 2, 1$



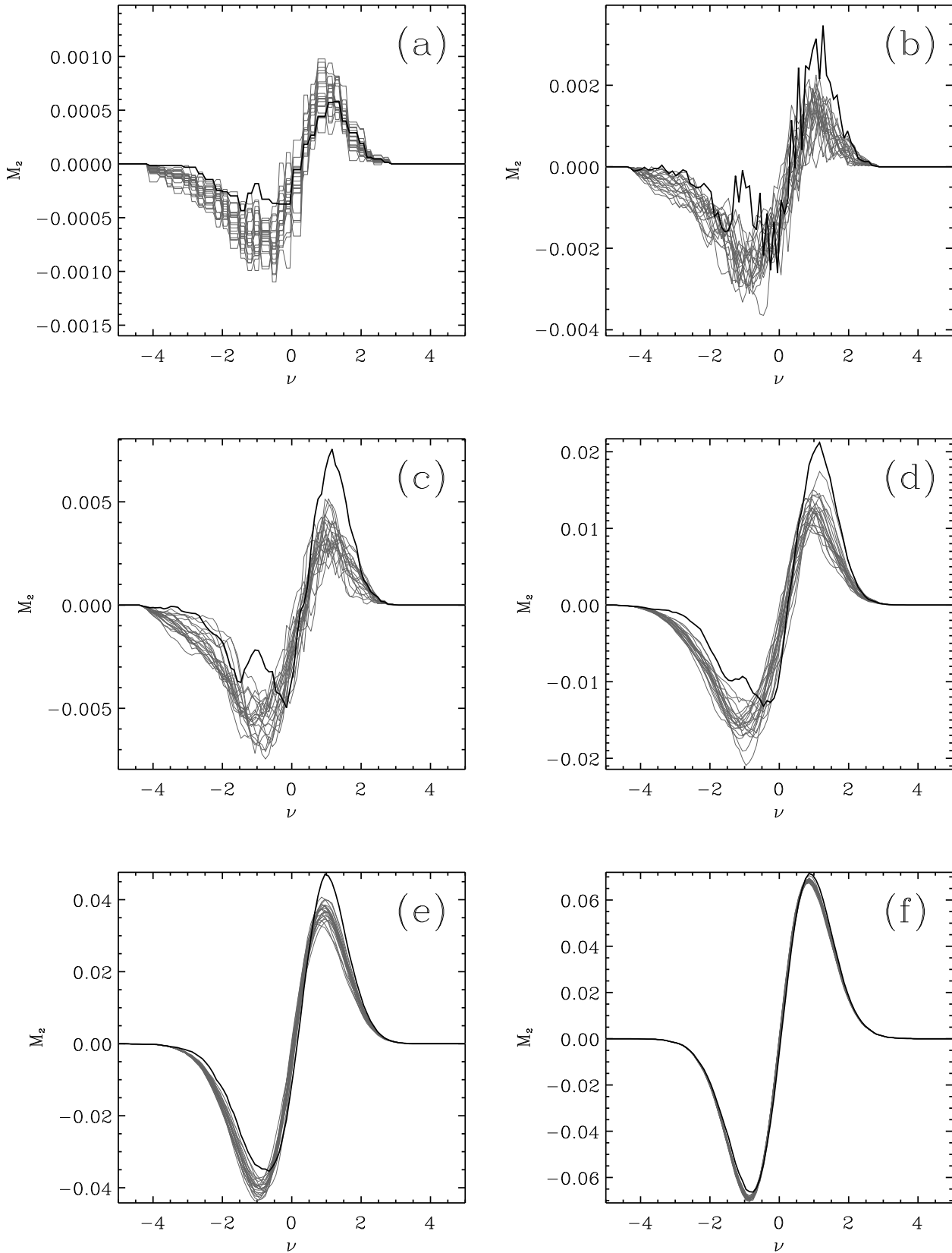


**Figure 12.** Minkowski functional  $M_2$  of the original image and the surrogates. Panel (a) is for the pure temperature map. Panel (b), (c), (d), (e) and (f) are the graphs for the combined map of CMB and additive white gaussian noise with SNR = 8, 4, 2, 1 and 0.5, respectively.